LAWRENCE
LIVERMORE
NATIONAL
LABORATORY

LLNL-JRNL-676315

Midplane neutral density profiles in the National Spherical Torus Experiment

D. P. Stotler, F. Scotti, R. E. Bell, A. Diallo, B. P. LeBlanc, M. Podesta, A. L. Roquemore, P. W. Ross

August 14, 2015

Physics of Plasma

Disclaimer

Midplane neutral density profiles in the National Spherical Torus Experiment

D. P. Stotler,[1] F. Scotti,[2] R. E. Bell,[1] A. Diallo,[1] B. P. LeBlanc,[1] M. Podestà,[1] A. L. Roquemore,[1] and P. W. Ross[1]

[1)] *Princeton Plasma Physics Laboratory, Princeton University, P. O. Box 451, Princeton, NJ 08543-0451, USA*[a)]

[2)] *Lawrence Livermore National Laboratory, Livermore, CA 94551, USA*

Atomic and molecular density data in the outer midplane of NSTX [Ono et al., Nucl. Fusion **40**, 557 (2000)] are inferred from tangential camera data via a forward modeling procedure using the DEGAS 2 Monte Carlo neutral transport code. The observed Balmer-β light emission data from 17 shots during the 2010 NSTX campaign display no obvious trends with discharge parameters, such as the divertor Balmer-α emission level or edge deuterium ion density. Simulations of 12 time slices in 7 of these discharges produce molecular densities near the vacuum vessel wall of 2 to 8×10^{17} m^{-3} and atomic densities ranging from 1 to 7×10^{16} m^{-3}; neither has a clear correlation with other parameters. Validation of the technique, begun in an earlier publication, is continued with an assessment of the sensitivity of the simulated camera image and neutral densities to uncertainties in the data input to the model. The simulated camera image is sensitive to the plasma profiles and virtually nothing else. The neutral densities at the vessel wall depend most strongly on the spatial distribution of the source; simulations with a localized neutral source yield densities within a factor of two of the baseline, uniform source, case. The uncertainties in the neutral densities associated with other model inputs and assumptions are $\leq 50\%$.

PACS numbers: 52.25.Ya, 52.55.Fa, 52.70-m, 52.65.Pp

[a)] Electronic mail: dstotler@pppl.gov

I. INTRODUCTION

The densities of neutral atoms and molecules in the main chamber of tokamaks are required to estimate their effects on particle, momentum, and energy balance (e.g., Ref. 1), on the formation of the H-mode pedestal,[2] and on the stabilization of plasma turbulence.[3] Midplane neutral densities in particular are needed to determine charge exchange losses of neutral beam ions;[4,5] to quantify fluxes of energetic charge exchange atoms to the main chamber wall, along with the associated sputtering;[6] and in the interpretation of edge diagnostics [e.g., charge exchange recombination spectroscopy (CHERS)[7]].

Multiple measurements of the neutral deuterium atom density have been made previously.[1,8–10] The most common technique infers the density via an inversion of the light measured by a calibrated camera. For example, Ross[5] used the Balmer-β line with the volumetric rate of light emission S_β being given by:

$$S_\beta = n_{\rm D}(1s)\left[\frac{n_{\rm D}(n=4)}{n_{\rm D}(1s)}\right] A_{4\to 2} \equiv n_{\rm D} F(n_e, T_e), \tag{1}$$

where $n_{\rm D}(1s)$ is the density of the deuterium ground state, the function F, representing the ratio of the density of the upper state of the transition to the ground state, is obtained from a collisonal radiative (CR) model,[11] and $A_{4\to 2}$ is the Einstein coefficient for the transition. If n_e and T_e are available from some other diagnostic covering the same volume in which S_β is measured, the value of F can be determined, giving

$$n_{\rm D} = S_\beta / F(n_e, T_e). \tag{2}$$

The first difficulty with this approach is that S_β and F are significant only over a relatively narrow radial region of the edge plasma. Farther out, where $n_{\rm D}$ is largest, n_e and T_e are too low to excite the upper state of the transition; farther in, $n_{\rm D}$ is reduced by ionization. In both cases, the signal S_β is small and likely dominated by noise. The second difficulty is in determining S_β from the line integrated measurements. Doing so via Abel inversion[12] requires assuming that S_β is only a function of major radius.

Direct modeling of the main chamber neutral density is also problematic since the dominant source of neutral molecules is usually recycling at the divertor targets. The first step in reconstructing that source is assembling a consistent characterization of the divertor plasma constrained by the available diagnostic data, a time consuming task that may or may not

yield a satisfactory result.[13] Once this is done, one would need to simulate the flow of the neutrals through the scrape-off layer (SOL) plasma to the vicinity of the midplane. Because the far SOL plasma is poorly diagnosed in most tokamaks, only rough estimates can be made of the attenuation of the neutral flux due to ionization. Furthermore, the main chambers of most tokamaks are geometrically complex, possessing 3-D vessel structures behind which neutrals can flow (Fig. 1). Main chamber recycling of large amplitude "blobs" striking the vessel wall represents another potentially significant source of neutrals.[14] Because this source is inadequately characterized and possibly toroidally asymmetric, estimates of its magnitude are highly uncertain.

We employ here a forward modeling technique[15] motivated by the success of a similar approach in the quantitative simulation of the neutral gas cloud in NSTX midplane gas puff imaging experiments.[16] Namely, we use the DEGAS 2 Monte Carlo neutral transport code[17] to invert D_β emission data from the tangentially viewing Edge Neutral Density Diagnostic (ENDD) camera.[5] Initial results for the simulation of two shots and some initial sensitivity studies were featured in Ref. 15. In the present work, we consider a wider range of experimental data and examine many more simulations. We also continue the validation of the method, begun in Ref. 15, with a detailed analysis of the uncertainties in the ENDD radial profile and the inferred neutral density profiles.

Section II describes the simulation technique and the underlying assumptions. The experimental database is discussed in Sec. III. The baseline simulations and resulting neutral density profiles are presented in Sec. IV. Experimental sources of uncertainty are examined in Sec. V, followed by those associated with simulation assumptions. The results of Sec. IV are discussed in the context of these uncertainties in Sec. VII.

II. SIMULATION METHOD

The ENDD system was originally designed to allow a simple inversion of Eq. (2) via an absolutely calibrated camera looking tangentially through the edge of the NSTX plasma,[5] providing radial profiles with 1.6 mm spatial resolution. The exposure time for each frame is 3.7 ms, or 268 frames per second. The camera image has 128×127 pixels, although vignetting and light reflections restrict this view to 123 pixels in the radial direction (20 cm), and 66 pixels poloidally (9 cm; the view is slightly oblique). As is discussed in Ref. 15,

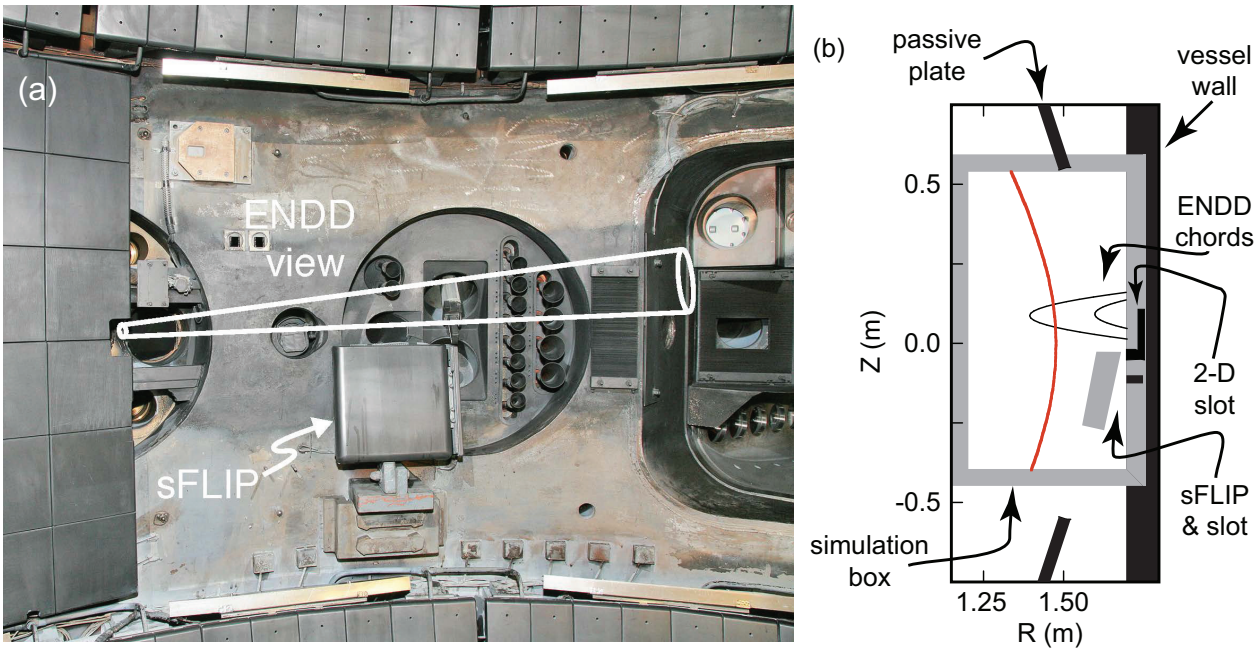

FIG. 1. (a) Schematic representation of the view of the ENDD camera showing adjacent hardware structures, including the sFLIP diagnostic, passive plates (tiled surfaces upper and lower), and the neutral beam armor (on left). (b) Corresponding view in the poloidal plane, showing the relative locations of the separatrix (red; shot 139412), two ENDD chords (innermost and outermost from the central horizontal row), the sFLIP diagnostic with gas pressure slot, and gas pressure slot for axisymmetric simulations. The locations of the upper and lower passive plate tiles (not simulated) are included for comparison. Reprinted with permission from D. P. Stotler, F. Scotti, R. E. Bell, B. P. LeBlanc, and R. Raman, J. Nucl. Mater. **463**, 897 (2015). Copyright (2015) Elsevier.

variation of the signal in this poloidal direction is small and will be ignored. The location of the ENDD view relative to other in-vessel structures is indicated schematically in Fig. 1.

The geometry used in the DEGAS 2 simulations is similar to that described in Refs. 16

and 18 and is based on contours of constant poloidal magnetic flux, from an NSTX EFIT equilibrium,[19,20] drawn inside a toroidally axisymmetric rectangle encompassing the emission volume viewed by the ENDD camera. The outer boundary of this rectangle corresponds to the vacuum vessel wall (Fig. 1); the inner boundary at $R = 1.2$ m is inside the penetration depth of all but the most energetic atoms. The passive plates are too far from the ENDD field of view for recycling there to contribute to its signal. We thus exclude them from the simulation box by limiting its vertical extent to $Z = -0.40 \rightarrow 0.54$ m, simplifying the geometry in the process.

The electron density and temperature profiles input to DEGAS 2 are derived from Thomson scattering[21] data as in Ref. 16, except that we use the CHERS diagnostic to estimate values for n_D^+/n_e and T_i/T_e. For the shots described in this paper, T_i does not differ from T_e significantly, and we assume $T_i = T_e$. The plasma profiles are assumed to be radially constant outside the outermost Thomson scattering point ($R = 1.56$ m).

The results in Ref. 15 came largely from 3-D simulations extending 103 degrees toroidally, 15 degrees beyond the ENDD view in both directions. The principal motivation for incorporating toroidal variation into the calculations was to assess the impact of recycling off of the Scintillator Fast Lost Ion Probe (sFLIP)[22] diagnostic, just below the ENDD field of view, to the simulated light emission. The conclusion drawn in Ref. 15 is that this is negligible; the bulk of the simulations since then have been axisymmetric; that is, without the sFLIP structure.

The simulations also contain "slots" (Fig. 1) shielded from the plasma to allow for the determination of a vacuum vessel density that can be compared with similarly shielded micro-ion gauges.[23] However, the data provided by those gauges in the discharges examined are noisy and have other limitations. In Ref. 15, we were only able to distill from them a range of densities and show that the simulated values are consistent with this range.

The primary difference between the present technique and that described in Refs. 16 and 18 is that the neutral source is not known here. In the absence of any additional information, we simply postulate a uniform, axisymmetric source of deuterium molecules coming off of the vacuum vessel walls with a thermal distribution at 300 K and a cosine angular distribution. The flux from this surface is assigned an arbitrary magnitude of 10^{20} $D_2/(s\ m^2)$. We will demonstrate in Sec. VI A that the simulated ENDD signal is insensitive to the spatial distribution of the source.

The atomic physics model used in these simulations is the same as that in Ref. 16 with two modifications. First, the volumetric source of D_β photons, computed via Eq. (1), is accumulated in each computational zone along the atoms' paths; a synthetic ENDD image is constructed from these data in post-processing. Second, we have updated the CR model used in Ref. 16, which was based on Ref. 24 with cross sections from Ref. 25, to incorporate new $n = 1 \rightarrow 3$, 4, and 5 excitation cross sections obtained from Convergent Close Coupling calculations.[26,27] The effects of this change are quantified in Sec. VI B 1.

As was shown in Ref. 28, Balmer-α photons arising from dissociative excitation and dissociative recombination make significant contributions to the signal recorded by GPI cameras, e.g., 40% at the emission peak in those simulations. The simulations in Ref. 15 ignore Balmer-β contributions from those processes. In Sec. VI B 2 we estimate their contributions to the simulated ENDD image using a preliminary model that can be implemented as a modest extension of the existing atomic physics model. Namely, we add Balmer-β photons in a manner parallel to that used for generating Balmer-α photons:[28,29]

$$\mathrm{e} + \mathrm{D}_2 \rightarrow \mathrm{e} + \mathrm{D}(1\mathrm{s}) + \mathrm{D}^*(n = 4), \tag{3}$$

$$\mathrm{e} + \mathrm{D}_2^+ \rightarrow \mathrm{e} + \mathrm{D}^+ + \mathrm{D}^*(n = 4), \tag{4}$$

$$\mathrm{e} + \mathrm{D}_2^+ \rightarrow \mathrm{D}(1\mathrm{s}) + \mathrm{D}^*(n = 4). \tag{5}$$

The rate for Eq. (3) is based on the model and data described in Ref. 30, evaluated in the low density, coronal limit. We estimate the rate for Eq. (4) from the corresponding Balmer-α rate[28] using the n^{-3} scaling suggested by Ref. 31. Reference 32 provides explicit data for Eq. (5).

The results described in Sec. IV are obtained by comparing a single horizontal row of pixels at the center of the simulated ENDD signal, 9 cm above midplane, with a corresponding row from the experimental imaged smoothed by binning over 10 adjacent vertical pixels (1.4 cm) to mitigate electronic noise from the camera. The ratio of the peak brightness in the ENDD signal, in photons / (s sr m^2), to that of the DEGAS 2 simulated signal provides an overall scale factor that can then be applied to all of the DEGAS 2 output, since the system is linear in the neutral distribution function, and to the neutral atom and molecular densities, in particular.

As will be demonstrated in sections V and VI, the radial location of the simulated ENDD peak is extremely insensitive to simulation assumptions. Hence, we use the difference be-

tween the observed and simulated peak locations: $\Delta R \equiv R_{\mathrm{ENDD}} - R_{\mathrm{DEGAS2}}$, where R_{ENDD} (R_{DEGAS2}) is the major radius corresponding to the peak in the observed (simulated) brightness profile, as the principal measure of the accuracy of the simulation in reproducing the experimental image. The uncertainties associated with both R_{ENDD} and R_{DEGAS2} will be quantified in Sec. V. Other measures, such as width,[18] can be considered in general.

The integration time of the ENDD camera of 3.7 ms is long compared to blob transport time scales[33,34] and can even encompass multiple small scale ELMs (NSTX type V ELMs have frequencies in the 300 - 800 Hz range[35]). However, the bulk of the discharges used here are from lithium-conditioned H-modes and are ELM-free.[36] One of the shots simulated (139412) has ELMs throughout most of the discharge. However, the time intervals simulated are during lulls in ELM activity.

Analysis of NSTX GPI experiments shows that the level of turbulent fluctuations in H-mode is below that in Ohmic and L-mode.[33] Some turbulent structures are nonetheless present. The neutral deuterium density profiles are the result of atoms propagating radially across the scrape-off layer, effectively averaging over these structures, both temporally and spatially, along the way. Consequently, we expect that the neutral density profile computed by a steady state neutral transport simulation will not differ significantly from the actual (i.e., temporally varying) profile. Methods of accounting for the effects of plasma turbulence on neutral penetration[37] have been developed and could be applied in a future analysis.

III. EXPERIMENTAL DATABASE

The data available for this study are limited to those run days in which the ENDD camera was fitted with a D_β filter and the camera was set to the *f*-stop used in the post-run calibration. From this set of discharges, we select shots having relatively steady total plasma energy, without radio frequency heating or large MHD modes during the flat-top, and then identify time ranges during those flat-tops without external fueling puffs or resonant magnetic perturbations (RMP).[38] The resulting database contains 184 time slices (33 ms apart, using every other Thomson scattering profile) in 17 discharges. As noted above, most of these plasmas are in H-mode. L-mode data are few since standard NSTX operation involves early neutral beam injection with correspondingly early L-H transitions; the ENDD signal during this portion of the discharge is also frequently contaminated by low field side

gas fueling. The full database is provided online. The toroidal magnetic field is 0.4 T in most cases with some discharges at 0.5 T. Similarly, the plasma current values are clustered around 0.8 MA with a few at 0.9 MA. A greater variety of plasma shapes are represented with elongations ranging between 2 and 2.5 and triangularity between 0.4 and 0.8. These result in a correspondingly large range of safety factors, with q_{95} extending between 6 and 12.

The maximum electron density in the Thomson scattering profiles varies between 3×10^{19} and 1×10^{20} m^{-3}. In virtually all shots, the electron density is increasing in time, perhaps in an off-axis peak, due to carbon accumulation;[39] the deuterium ion inventory does not increase in a similar manner.[40] The maxima of the electron temperature profiles range from 0.7 to 1.5 keV. The peaks of the calibrated, inverted ENDD emissivity profiles vary between 5.4×10^{18} and 3.6×10^{19} photons / (m^3 s). The peak emissivity has no obvious correlation with the other parameters, including divertor D_α emission rate. There is a weak trend for the emissivity to decrease with the maximum electron density, but to increase with the edge deuterium ion density (Fig. 2). The latter is estimated using the outermost CHERS C^{6+} density via $n_{D^+} \simeq n_e - 6n_{C^{6+}}$; this is at $R = 1.46$ m, slightly less than the bulk of the R_{ENDD} values.

IV. RESULTS

We simulate twelve time slices in seven shots from this database. In Fig. 3, we compare the simulated and observed ENDD brightness profiles from shots 139412 and 142214, both at 0.4 s into the discharge. As was the case with the corresponding three-dimensional simulations in Ref. 15, we argue that their similarity, $\Delta R = -0.3$ cm, provides an initial confirmation of our approach to inverting the ENDD data and of the adequacy of the uniform D_2 source ansatz.

The simulated peak locations, R_{DEGAS2}, track very closely the steep gradient region in the plasma profiles. This is depicted in Fig. 4, using the radius at which $T_e = 100$ eV, R_{100}, as a proxy for the steep gradient location. Note that this is at midplane, while the ENDD radii are effectively at $Z = 9$ cm. Mapping between the two produces a shift of 0.5 to 2 cm, depending on the flux surface shape. Consequently, the simulated emission peaks at some $T_e < 100$ eV; determining a precise value is difficult due to the steepness of the plasma

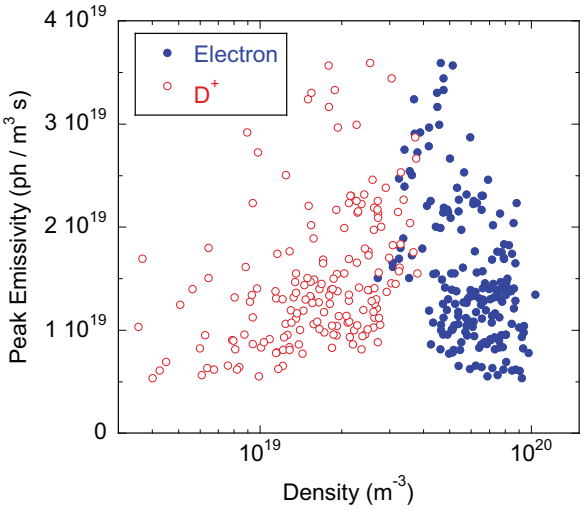

FIG. 2. Relationships between the peak of the ENDD emissivity profiles for all time slices and the maximum electron density (from Thomson scattering profiles) and edge deuterium ion density (from CHERS).

gradients and the limited spatial resolution of the profiles and the simulation.

The values of ΔR vary over the entire set of simulations, -1 cm $< \Delta R < 4$ cm. Those variations do not appear to be random; in particular, they decrease with increasing R_{100} (Fig. 4). At the same time, the ENDD peak emissivity (same data as in Fig. 2) increases with R_{100}. A plausible, simple explanation for the latter is that neutral densities would be expected to be larger closer to the vessel wall. However, the correlation may also be a side effect of the phenomenon or phenomena responsible for the larger ΔR values; this will be discussed further in Sec. VII.

The neutral source scaling factor for the two simulations in Fig. 3 is determined to be 2.5 (1.6) for 139412 (142214). The resulting scaled radial profiles of the D and D_2 densities at midplane ($Z = 0$), extracted from the simulation volume, are shown in Fig. 5. As will be discussed in Sec. V B 2, the magnitude and shape of the neutral density profiles near the wall at $R = 1.7$ m depend on the assumed plasma profiles beyond the outermost Thomson scattering point ($R = 1.56$ m). For comparison, we have included in Fig. 5 the D density

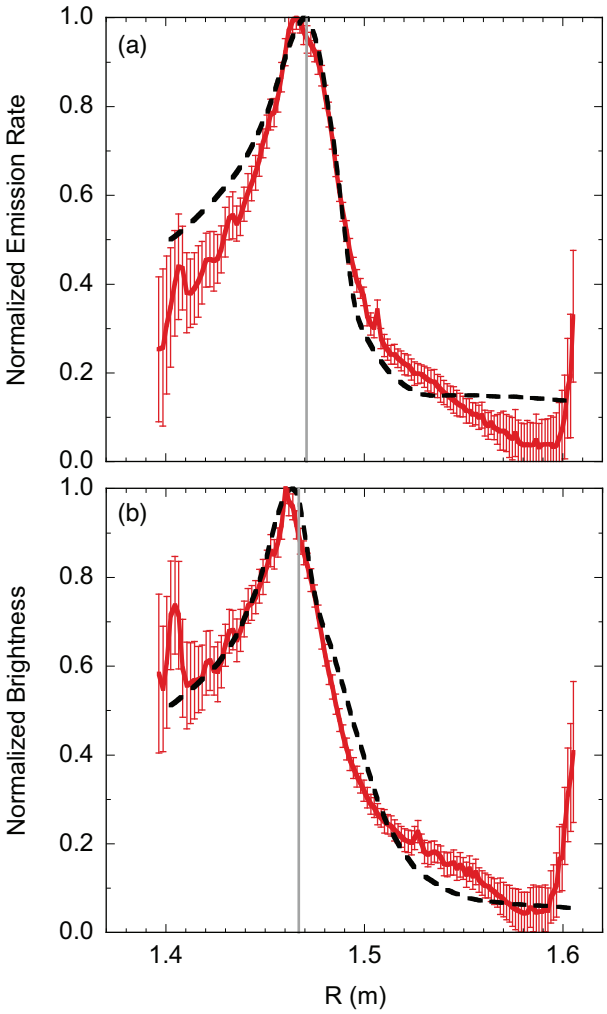

FIG. 3. Simulated (dashed) and observed (solid) radial ENDD profiles of line integrated Balmer-β brightness for shots (a) 139412 and (b) 142214, all normalized to maximum values of unity. The horizontal axis corresponds to the tangency radius of each pixel chord as obtained via Abel inversion.[12] The gray lines indicate the separatrix location at the Z coordinate of the ENDD view. The error bars on the experimental profile are associated with the calibration of the ENDD camera. Reprinted with permission from D. P. Stotler, F. Scotti, R. E. Bell, B. P. LeBlanc, and R. Raman, J. Nucl. Mater. **463**, 897 (2015). Copyright (2015) Elsevier.

profile for shot 142214 computed from Eq. (2), following an Abel inversion[12] to obtain S_β.

The overall range of neutral densities, both atomic and molecular is shown in Fig. 6 (circles). Since the D_2 source is at the wall, the molecular density peaks there as well. The location of the peak in the atom density and the amount by which it exceeds the density at the wall hinge on the SOL plasma parameters. The molecular densities range from 2×10^{17}

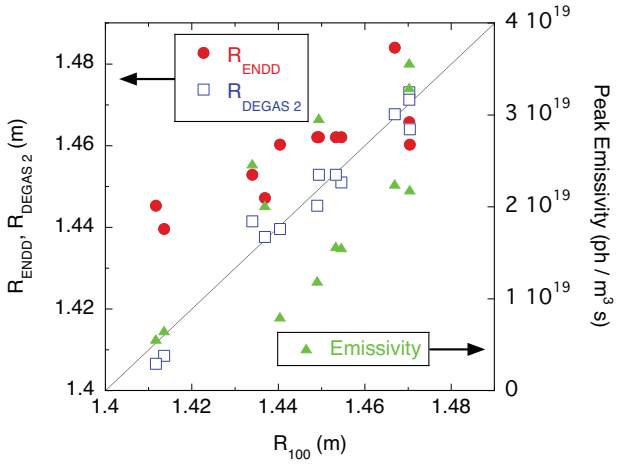

FIG. 4. Simulated (R_{DEGAS2}; squares) and observed (R_{ENDD}; circles) locations of the peaks in the ENDD profiles as a function of the midplane major radius at which $T_e = 100$ eV, R_{100}. The peak emissivity (triangles, right axis) tends to increase with R_{100}.

to 9×10^{17} m^{-3}; roughly speaking, on the order of 10^{17} m^{-3}. The maximum atom densities vary from 1×10^{16} to 7×10^{16} m^{-3}, i.e., generally $\sim 10^{16}$ m^{-3}. The radial profiles all qualitatively resemble those in Fig. 3. Note that this range of molecular densities is very similar to that inferred from midplane micro-ion gauge data in Ref. 15. As with the peak emissivity, there are no clear correlations of these densities with other discharge parameters, such as the divertor D_α or the edge deuterium ion density. Note, however, that this set of 12 simulations represents a much smaller, and less than comprehensive, database than that of Fig. 2.

V. EXPERIMENTAL SOURCES OF UNCERTAINTY

A. ENDD System

The principal contributor to the uncertainty of the ENDD signal is its calibration. Because the maximum ENDD brightness is used to calibrate the source in the simulations, this uncertainty translates to a corresponding overall uncertainty in the magnitude of the

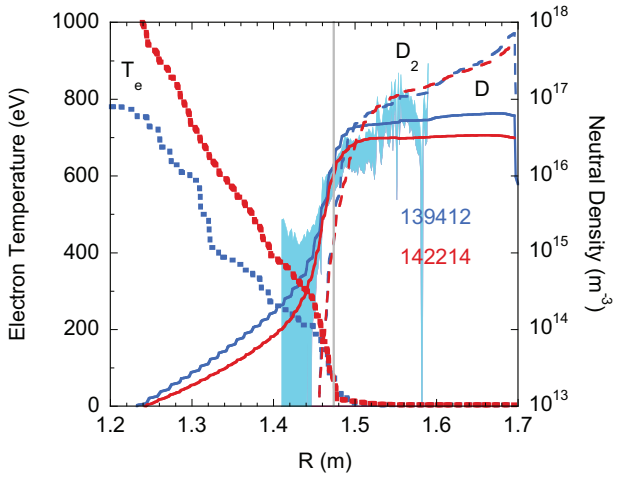

FIG. 5. Inferred deuterium atom (solid lines) and molecule (dashed lines) midplane density profiles for NSTX shots 139412 and 142214, both at 0.4 s. The electron temperature profiles (dotted lines) are provided for reference. The gray line indicates the separatrix location (same for both shots). The shaded area represents the atom density for shot 142214 inferred from the inverted ENDD signal via Eq. (2); the vertical width indicates the propagated uncertainty associated with the ENDD camera calibration. Reprinted with permission from D. P. Stotler, F. Scotti, R. E. Bell, B. P. LeBlanc, and R. Raman, J. Nucl. Mater. **463**, 897 (2015). Copyright (2015) Elsevier.

inferred neutral density.

The absolute calibration of the system was performed *in situ* with an integrating sphere and a white-plate target. The calibration uncertainty is obtained from the standard deviation of the sensitivity at each of the 20 central, vertical pixels (55 to 74) relative to their radially smoothed average. The relative sensitivity of the camera across the frame and the associated uncertainty are plotted in Fig. 7, along with the brightness data for shot 142214 for reference. Note in particular the drop in sensitivity due to vignetting at smaller major radii, where the bulk of the brightness peaks are found. These uncertainties are shown also in Fig. 3 (3% at the emission peak) and propagated through the inversion process, resulting in the error bars depicted in Fig. 5.

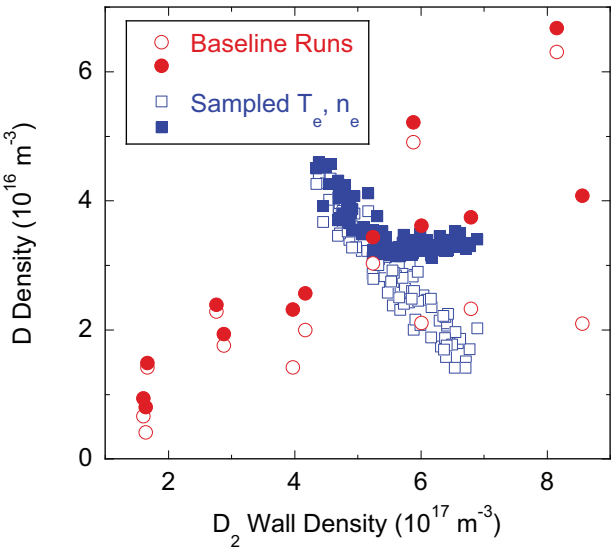

FIG. 6. Range of atomic (vertical axis) and molecular (horizontal axis) densities for all baseline simulations (red circles). Both the atomic densities at the wall (closed symbols) and profile maxima (open symbols) are depicted. The blue squares are the atomic and molecular densities for the 100 simulations with the Monte Carlo sampled n_e and T_e profiles of shot 142214 at 0.4 s, described in Sec. V B 1.

The spatial calibration of the camera was carried out *in situ* via two target plates placed in the field of view. Images of these plates were recorded, then the spatial coordinates of specific points on these plates were determined via a measuring arm. The corresponding pixel coordinates were then established from the image; their estimated uncertainty is 0.5 pixels $\simeq$ 0.8 mm. With these data, planes are fit to the measured points and real space lines are constructed for the path of each camera pixel through the field of view; these chords are used to construct the synthetic ENDD diagnostic in DEGAS 2. The tangency radius of each chord is determined for use in plotting camera data as a function of major radius (e.g., as in Fig. 3). The error in the plane fits is roughly 2.5 mm. When combined with the uncertainty in the pixel coordinates, we get an overall uncertainty in the spatial calibration of 3 mm.

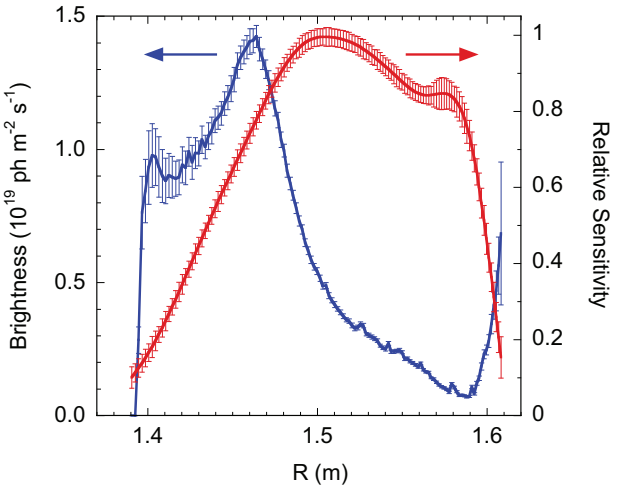

FIG. 7. Relative sensitivity of the ENDD imaging system is plotted on the right axis. The ENDD brightness profiles for shot 142214 is included for reference.

An uncertainty not accounted for in the calibration is the blue-shift of the central wavelength of the interference filter band-pass due to oblique incidence of off-axis light rays. In the ENDD setup, the D_β interference filter was positioned in front of the imaging lens. The incident angle of the most off-axis ray imaged on the sensor, at the central vertical position used for the ENDD analysis, is given by $\tan^{-1}(\frac{l}{2f})$, where l is the sensor size (4 mm) and f is the focal length of the imaging lens (25 mm). The filter transmission was re-calibrated with a spectrometer (central wavelength 4859.4 Å, FWHM 14.1 Å), and the effect of the blue-shift on the ENDD sensor was estimated to be at most 4 Å. This would result in an 8% correction in the relative sensitivity at the extremes of the ENDD field of view. This is too small to alter the location of emission peak.

The mirror providing the camera's view into the torus was exposed to lithium evaporation throughout the 2010 campaign and, prior to calibration, developed a white stripe on it as result of the reaction of lithium with air. The light striking this location on the mirror should be well out of focus and, thus, is expected to not have a significant effect.

B. Plasma Profiles

The other principal inputs to the method are the plasma profiles obtained via the Thomson scattering diagnostic. We also consider ion density and temperature data from the CHERS system, but find that the simulation results are insensitive to those values (Sec. VI B 3). Obtaining accurate electron density and temperature data requires densities above a few times 10^{17} m^{-3}. However, the SOL densities are typically less than this, and the reported electron densities and temperatures are thus unreliable. As noted in Sec. II, the outermost viable values are extrapolated through the rest of the profile as constants.

1. Monte Carlo Sampling of Plasma Profiles

Associated with the Thomson scattering plasma parameters are estimated errors in value, from both random and systematic errors, and spatial location, due to the finite size of the volume sampled by the laser and optical system.[21] We construct 100 different profiles for shot 142214 at 0.4 s, randomly sampling both the radial location (from a uniform distribution) and the value (from a Gaussian distribution) at each Thomson scattering point. We then perform an axisymmetric DEGAS 2 simulation with each profile.

The resulting peak locations vary between pixel locations 32 and 41, corresponding to a range of 1.4 cm, with a mean of 36 (same as the baseline) and a standard deviation of 2.0 pixels $\simeq$ 0.3 cm. The FWHM of the peak has a mean value of 50 pixels, again matching the baseline, and a standard deviation of 5 pixels $\simeq$ 0.8 cm.

The overall scaling factor for each simulation is determined, as in Sec. II, by dividing the maximum simulated brightness into the observed ENDD brightness peak. These factors are then used to rescale the neutral density profile extracted from the simulation output. Those maximum and wall densities are summarized in Table I and depicted in Fig. 6.

2. Sensitivity of Densities to SOL Parameters

No direct measurements of the plasma parameters are available between the outermost Thomson scattering point at $R = 1.56$ m and the vessel wall at $R = 1.70$ m. As noted above, many of the discharges simulated have no accurate measurements of the plasma parameters in the SOL at all due to too low density or passing intermittent turbulent

TABLE I. Mean and standard deviations of parameters determined from 100 Monte Carlo sampled Thomson scattering profile simulations of shot 142214 at $t = 0.4$ s. Note that the deviation in peak location corresponds to a radial distance of 0.3 cm. Also, the molecular density peaks at the wall.

Parameter	Mean	Std. Dev.
Peak location (pixel)	36	2.0
FWHM (pixel)	51	5.0
Maximum n_{D} (m^{-3})	3.5×10^{16}	3.7×10^{15}
Wall n_{D} (m^{-3})	2.9×10^{16}	7.5×10^{15}
Wall n_{D_2} (m^{-3})	5.5×10^{17}	6.6×10^{16}

structures ("blobs").

The $t = 0.4$ s Thomson scattering profile for 142214 has $n_e > 10^{18}$ m^{-3} everywhere with correspondingly small uncertainties ($\Delta T_e/T_e \leq 31\%$, $\Delta n_e/n_e \leq 15\%$); this is likely one reason the simulation so closely matches the observed ENDD profile. These relatively small uncertainties also make this shot and time an ideal candidate for assessing the sensitivity of the simulations to SOL plasma parameters. In fact, the Monte Carlo sampling of those profiles in Sec. V B 1 does precisely that.

The Thomson scattering data used in Sec. V B 1 are extrapolated as constant from $R = 1.56$ out to the vessel wall, as in the baseline simulations. The sampling yields electron temperatures and densities in the ranges $T_e = 1.9 \rightarrow 6.7$ eV and $n_e = 8.3 \times 10^{17} \rightarrow 1.7 \times 10^{18}$ m^{-3}. Between these two T_e, the D_2 dissociation reaction rate increases by over a factor of 50, with a corresponding decrease in the molecular mean free path. For this reason, both the simulated atomic and molecular densities are relatively sensitive to the input T_e. For these same SOL parameters, the ionization mean free path of the ~ 3 eV atoms produced by dissociation is much longer. Thus, the primary sink for SOL atoms in these simulations is transport. The dependence of the density profiles on the SOL T_e is depicted in Fig. 8. Note again that these are the *scaled* neutral densities that take into account the variation in the simulated ENDD brightness. In the higher T_e runs, dissociation occurs closer to the wall, resulting in reduced D_2 density at $R = 1.6$ m and a larger D density at the wall. Because the SOL n_e varies over a smaller range and enters the reaction rate only linearly, the dependence of the densities on it cannot be discerned in the data. The resulting variation in the atomic

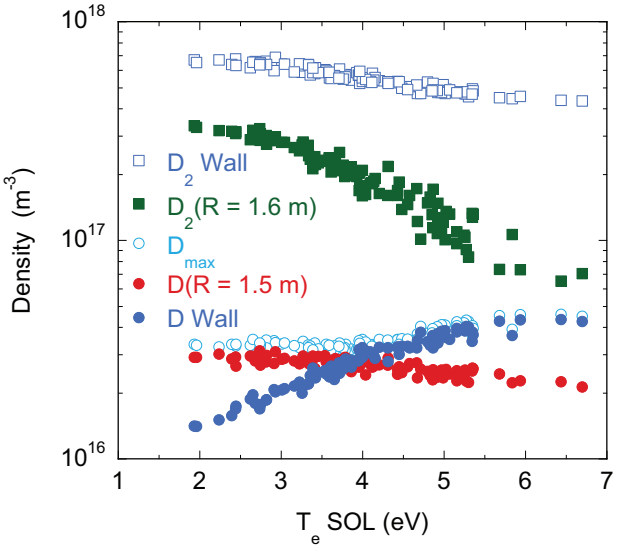

FIG. 8. Relationship between neutral densities and the assumed SOL electron temperature in the Monte Carlo sampled simulations described in Sec. V B 1. Molecular densities at the wall ($R = 1.7$ m) and at $R = 1.6$ m are shown. The maximum atomic density over the profile, D_{max} is depicted, as are the values at $R = 1.5$ and 1.7 m.

and molecular densities at the wall is characterized by the standard deviations shown in Table I; they correspond to 26% and 12% of the mean values.

Note that the atom density at $R = 1.5$ is much less sensitive to the SOL T_e, having a relative standard deviation of only 8%. The standard deviation of the the maximum atom density is 11%; a similar value applies at $R = 1.3$ and 1.4 m. In other words, the atomic and molecular densities in the confined plasma are relatively insensitive to the poorly determined SOL plasma parameters. A primary reason for this is that these radii are closer to the ENDD peak, where the atom density is effectively fixed by the calibration procedure. In contrast, the atoms near the wall are affected by the strong variations of the ionization and dissociation rates at typical SOL temperatures.

3. Plasma Motion

Motion of the separatrix during the relatively long exposure time of the ENDD camera and between Thomson scattering profiles contributes to the uncertainty in the simulated peak location. The motion of the separatrix between Thomson profiles is estimated to be up to 1 cm. There are also, on average, 4 ENDD frames between each Thomson scattering pulse so that their relative synchronization is also a factor. An examination of multiple Thomson scattering profiles in various shots and their relationship with the adjacent ENDD profiles results in a comparable centimeter-size uncertainty. We assign a combined uncertainty of 1 cm to these two related effects.

VI. SENSITIVITY TO SIMULATION ASSUMPTIONS

A. Sensitivity To Source Distribution

A principal assumption of the method described in Sec. II is the uniform distribution of the neutral source along the vacuum vessel wall. We assess the sensitivity of the simulated ENDD and neutral density profiles to this assumption by instead postulating spatially localized neutral sources in a series of simulations.

We first consider variants of the shot 139412 case in which the neutral source is a single segment of the vertical surface representing the vacuum vessel wall. Those locations are depicted in the inset of Fig. 9(b) and the resulting ENDD profiles in Fig. 9(a).

The average relative deviations of the normalized ENDD profiles from those of the baseline for the sources at $Z \geq -0.139$ m are $< 7\%$; for the case with source at $Z = -0.338$ m, the average relative deviation is 18%. The largest absolute deviation from the baseline of 0.05 arises in this last case as well. All of these differences are small in comparison with those seen in Fig. 3, indicating that the shape of the ENDD profile is relatively insensitive to the spatial distribution of the source. We suspect that the differences in Fig. 3 are instead the result of our inability to accurately reconstruct the plasma profiles, principally due to the limited spatial and temporal resolution of the NSTX Thomson scattering system.

The associated neutral density profiles are more sensitive to the source distribution. After calibrating the magnitude of the source via the observed maximum ENDD brightness, we obtain the absolute neutral density profiles shown in Fig. 9(b). If we restrict the radial

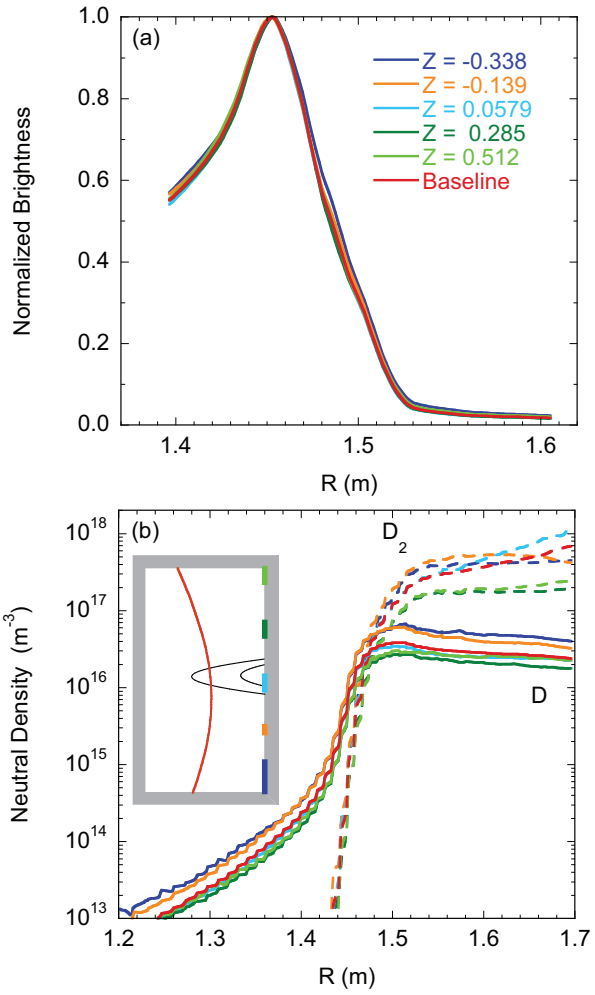

FIG. 9. Variation of (a) ENDD and (b) density profiles with source location on outer wall.

range of interest to that over which the baseline neutral density falls a factor of 10^5 from its maximum value, most of these densities are within a factor of two of the baseline. The exceptions are D_2 densities for the two higher Z locations near the wall; these are within a factor of three of the baseline.

A significant contributor to the variations in the density profiles is that they are taken over the volume $-0.05 \leq Z \leq 0.05$ m (i.e., around midplane) while the ENDD chords sample just above this, around $Z = 0.09$ m. This difference is comparable to the vertical scale lengths of the 2-D neutral density profiles in these isolated source cases. Keep in mind that these runs are artificial exaggerations designed to highlight the insensitivity of the ENDD profile to the source distribution. Their effect on the density profiles also sets an upper bound on the uncertainty of the density profiles due to the uniform source assumption. If we had

evidence that a spatially varying source is a more realistic characterization, specifying the density profiles at the same Z as the ENDD views would be more appropriate.

Similar conclusions follow from the scenario depicted in Fig. 10, based on shot 142214, in which the sources are instead located on lower boundary of the simulation volume. These cases are intended to mock up the direct penetration of neutrals from the divertor through the confined plasma rather than through the SOL. The average relative deviations in the ENDD profiles from the baseline is again $\leq 18\%$. The maximum absolute deviation of 0.08 arises at the small R edge of the frame in the run having the source at $R = 1.40$ m. Even deviations of this magnitude would be difficult to detect in a comparison with the observed profiles. All of the neutral densities for these runs, Fig. 10(b), are within roughly a factor of two of the baseline densities except for the D densities in the $R = 1.40$ m source location run, which deviates more strongly for $R < 1.45$ m. This part of the profile contains significant contributions from atoms penetrating directly through the plasma rather than through the SOL.

B. Sensitivity To Physics Model

1. Collisional Radiative Model

The details of the atomic physics models used in Monte Carlo neutral transport codes continue to advance, even for hydrogen, as is illustrated by the development of improved excitation cross sections in Ref. 27. The same is true of the collisional radiative models into which such data are incorporated (e.g., Ref. 41). To estimate the magnitude of the uncertainty associated with such changes, we quantify the effect of the revised $n = 1 \rightarrow 3$, 4, and 5 excitation cross sections (Sec. II) on the inferred neutral density. At its peak, corresponding to an electron energy of ~ 20 eV, the revised $n = 4$ excitation cross section[26,27] is roughly 50% smaller than the one used previously;[25] this difference decreases with increasing energy, vanishing at about 200 eV. The resulting Maxwellian averaged excitation rate is 45% smaller at $T_e = 10$ eV, dropping to 14% at 100 eV; similar reductions are seen in the $n = 4$ population coefficient $[n_{\rm D}(n = 4)/n_{\rm D}(1s)$ in Eq. (1)] from the CR model. The impact on the ionization rate is smaller, 10% or less.

Because of this, the unscaled D_2 and D neutral densities in simulations of shot 139412

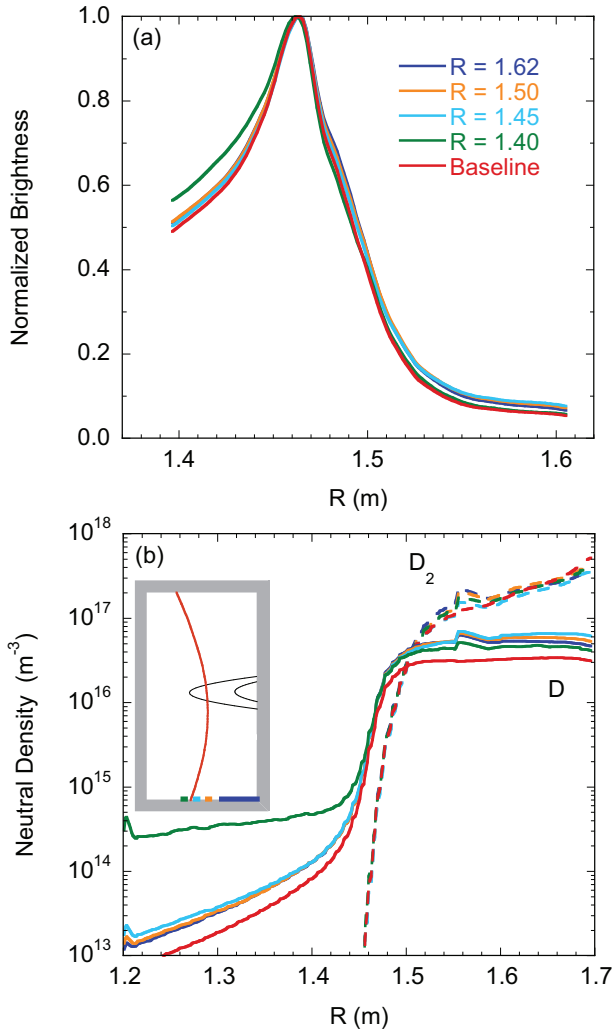

FIG. 10. Variation of (a) ENDD and (b) density profiles with source location on lower wall.

(Sec. IV) with the two CR radiative models are essentially the same. The peak simulated ENDD brightness, however, is 31% lower with the revised CR model due to its smaller $n = 4$ excitation rate. The overall calibration factor applied to the simulation source strength is inversely proportional to this quantity, so that the inferred neutral densities are $\sim$ 30% *higher* than one would have obtained via the previous CR model.

2. Molecular Contributions

We incorporate the molecular emission processes in Eqs. (3), (4), and (5) into the simulation of shot 142214 (Sec. IV) to estimate the magnitude of their contributions. At the peak of the ENDD profile, the molecular processes make up 35% of the total D_β emission, result-

ing in a 35% drop in the scaling factor. Their fractional contribution increases to $> 60\%$ in the lower temperature regions of the SOL where the molecular density greatly exceeds that of the atoms, broadening that part of the ENDD profile slightly. Because these processes are incorporated only as additional emission channels, the unscaled neutral densities are unaltered. Thus, the inferred neutral densities are 35% lower than in the baseline case.

An analogous simulation is performed for shot 140213 at $t = 0.45$ s, one of the two smaller R_{100}, larger ΔR cases in Fig. 4 ($R_{100} = 1.41$ m, $\Delta R = 3$ cm). The contributions from molecular processes are even larger in this run, 60% at the peak, rising to 80% near the vessel wall. These are big enough to shift the simulated emission peak outward by 2 cm. The scaling factor is reduced by 50%, with a corresponding drop in the neutral densities relative to the baseline simulation. This increased importance of molecular emission is the result of plasma parameters lower than those in shot 142214. However, the low electron densities ($< 3.5 \times 10^{17}$ m^{-3} for $R \geq 1.46$ m) are accompanied by large uncertainties in the Thomson scattering data. In fact, no viable T_e are available and we assume $T_e = 7$ eV for this range in radii.

These result suggests that the molecular contributions to the ENDD signal may be non-negligible, perhaps playing a larger role than they do in systems based on the D_α line. Their contributions may, thus, impact the overall profile shape and sensitivity to plasma parameters. However, this is a relatively simple treatment of the molecular processes that has not been as thoroughly validated as have the models for molecular D_α.[16,29,42] A more careful analysis would entail additional research into the cross sections for Eqs. (3), (4), and (5) and perhaps the use of a combined D, D_2 CR model.[43,44]

3. Charge Exchange / Elastic scattering

Theoretical investigations of neutral penetration in the literature emphasize the importance of charge exchange in the process.[2,45–48] However, the simulated ENDD is surprisingly insensitive to it. As a demonstration, we remove charge exchange from the list of reactions used in the simulation of shot 142214. The resulting maximum relative deviation in the simulated ENDD profile from the baseline (Fig. 3) is 19% and averages 12% over the full profile. The location of the peak shifts to smaller R, but only by a single pixel. The scaled neutral density profiles outboard of the emission peak are similarly unaffected, Fig. 11; the

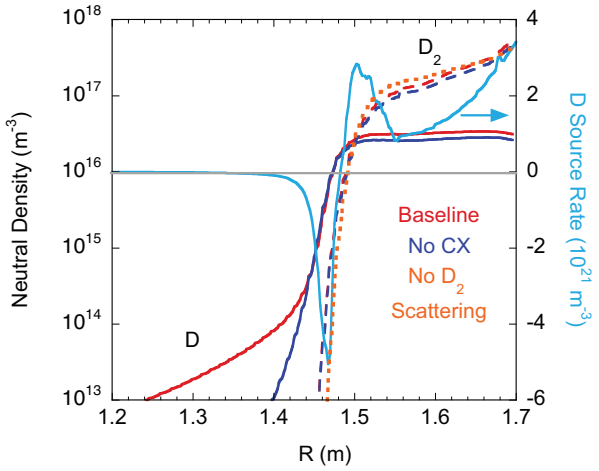

FIG. 11. Comparison of scaled neutral densities (left axis) in variants of the simulation of 142214 (red curves) without atom-ion charge exchange (blue curves) and without molecule-ion elastic scattering (orange dotted curve). The right axis depicts the volumetric source / sink rate of deuterium atoms in the baseline simulation across this radial slice

D_2 density at the wall drops 13%, the D density by 17%. The removal of charge exchange *does* significantly alter the profiles at major radii smaller than that of the emission peak. However, these differences are too small relative to the peak emission rate to be discerned in the ENDD profile.

This insensitivity to charge exchange arises even though the charge exchange rate in the baseline simulation of 142214 exceeds the ionization rate everywhere except for a narrow region around the emission peak; this is also the case in many of the other simulations. The dominant process for $R > R_{\mathrm{DEGAS2}}$ is instead the creation of D atoms by molecular dissociation, as is clear from their volumetric source rate, shown in Fig. 11. The relative strength and diffuse nature of this source prevents a simple analytic explanation of the radial variation of the D density profile in this region.

At smaller major radii, only charge exchange and ionization are active and analytic models *are* applicable. The D density scale length over this range of radii is shown in Fig. 12 ("Baseline") along with scale lengths estimated from analytic expressions. The most

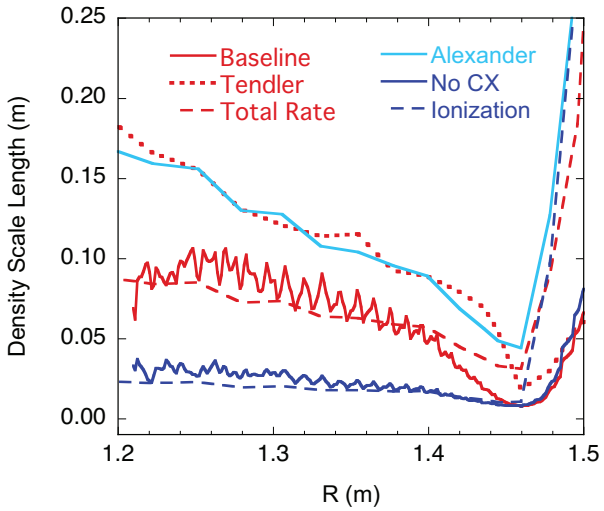

FIG. 12. Scale lengths for the deuterium atom density, $\lambda \equiv (d \ln n_{\rm D}/dR)^{-1}$, for the baseline simulation of shot 142214 (solid red line) and for the variant without atom-ion charge exchange (solid blue line). The scale length derived in Ref. 46 evaluated with the neutral thermal velocity equal to the ion thermal velocity is labeled "Tendler" (red dotted line). "Total Rate" (red dashed line) is a simpler variant, Eq. (6). The curve labeled "Alexander" (solid cyan) is computed using Eq. (7). The dashed blue line is the penetration length computed from the ionization rate at an energy of 3 eV.

complex of these is Eq. (14) in Ref. 46; this is the curve labeled "Tendler", evaluated with the ionization and charge exchange rate tables used in DEGAS 2, the plasma profiles from the simulation, and assuming that the neutral thermal velocity is the same as that of the ions. Strictly speaking, DEGAS 2 treats charge exchange via a differential elastic scattering cross section; the equivalent charge exchange reaction rate[49,50] is used for this analysis.

We find, however, that the atoms are not completely thermalized with the ions and that their relative temperatures might be better characterized as $T_{\rm D} = T_i/2$. Evaluating the charge exchange rate with this assumption and making a corresponding adjustment to the neutral thermal velocity, $v_{\rm th,D} \simeq \sqrt{T_i/m_{\rm D}}$, the Tendler scale length much more closely tracks

that of the simulation (not shown). An even simpler expression matches just as well:

$$\lambda_{\text{total}} = v_{\text{th,D}}/[n_i S_{\text{cx}}(T_i, E_D) + n_e S_{\text{ion}}(T_e, n_e)], \tag{6}$$

where S_{cx} and S_{ion} are the charge exchange and ionization reaction rates, respectively; this is "Total Rate" in Fig. 12. For comparison, we include another expression found in the literature;[48,51]

$$\lambda_{\text{Alexander}} = v_{\text{th,D}}/[n_e S_{\text{ion}}(n_i S_{\text{cx}} + n_e S_{\text{ion}})]^{1/2}; \tag{7}$$

this is significantly larger than both λ_{total} and the scale length inferred from the simulation. Because $S_{\text{cx}} > S_{\text{ion}}$ over this range of radii, the limiting expression from Ref. 48, $\lambda^{-1} \propto \sqrt{S_{\text{ion}} S_{\text{cx}}}$, is comparable to $\lambda_{\text{Alexander}}$. The scale length for the simulation without charge exchange ("No CX") is well described by $\lambda_{\text{ion}} = v_{\text{FC}}/n_e S_{\text{ion}}$, where v_{FC} is the velocity corresponding to the ~ 3 eV Franck-Condon atoms produced by dissociation ("Ionization").

Elastic scattering of D_2 on deuterium ions similarly increases molecular penetration in the divertor plasma (see, e.g., Ref. 52 and 53). But, the simulated ENDD profile is again insensitive to its removal, with maximum and mean relative deviations from the baseline of 13% and 6.5%, respectively. The effect on the D density profile is also modest, differing from the baseline by $< 10\%$. Removing this process from the simulation does reduce the maximum penetration depth of the molecules, analogous to the elimination of charge exchange above, Fig. 11. The resulting D_2 density at the wall is 19% lower than in the baseline.

4. Wall Model

Most models for the interactions of plasma and neutral particles with material surfaces are idealized and unrealistic characterizations of the ones that occur in actual tokamaks (see, e.g., Refs. 54 and 55). Further complicating matters, the NSTX vacuum vessel surface composition likely varied from shot-to-shot due to changes in the amount of lithium evaporated and even during a shot as a result of passivation of the coatings.[56]

Because our assumed neutral source is a gas puff coming from the walls, the particle-material interactions (PMI) in these simulations are a secondary consideration, invoked only when atoms are returned to the wall by a molecular dissociation or charge exchange event. However, because the bulk of the dissociations occur relatively close to the wall, this returning atom current is still half of the initial source.

TABLE II. Maximum and mean relative deviation in the normalized ENDD profiles, and differences in maximum and wall densities, relative to the baseline, in simulations assuming stainless steel wall and without desorption.

Variant	$\max(\Delta S_\beta/S_\beta)$	$\langle\Delta S_\beta/S_\beta\rangle$	$\Delta(\max n_{D_2})$	$\Delta\max n_D$	$\Delta n_{D,wall}$
Steel wall	13%	4%	−20%	13%	13%
No desorption	3%	1%	26%	−3%	−6%

The PMI model employed in these simulations is a standard combination of backscattering and desorption.[54] The backscattering probability and kinetic distribution of backscattered atoms are sampled from probability distributions contained in tables compiled from multiple runs of a binary collision algorithm code (BCA), such as TRIM.[57] In steady state, atoms not reflected are assumed to be absorbed, recombined into molecules, and then desorbed back into the plasma at the temperature of the material surface. With no net absorption, the principal product of the PMI model is the backscattering probability; it determines the relative fraction of fast atoms and cold molecules coming off of the wall.

The simulations in Sec. IV use a backscattering model developed for graphite (effectively carbon), first because graphite is the dominant plasma facing material in NSTX. Secondly, the extensive lithium evaporation and carbon redeposition during the run produced a variety of difficult-to-characterize surface coatings; carbon is a plausible intermediate between the low atomic weight of lithium and that of the stainless steel substrate. To assess the sensitivity of the simulations to the PMI model, we consider two extreme alternatives. In the first, we take the walls to be bare stainless steel, much as they would be at the beginning of a run campaign. In the second, we assume 100% absorption; only backscattered atoms return from the wall. Because this amounts to a relatively large sink of deuterium atoms, the overall scaling factor inferred by normalizing to the observed ENDD profile is roughly double its value in other runs. The deviations of the results from these simulations from the baseline simulation of shot 142214 are shown in Table II; these are all relatively modest.

VII. DISCUSSION AND SUMMARY

The dominant uncertainty in the simulation of the ENDD brightness profile is that associated with the input Thomson scattering profiles; the ENDD profiles are remarkably insensitive to all other simulation inputs and assumptions. The Monte Carlo sampling procedure described in Sec. V B 1 indicates an uncertainty in the peak location for a single Thomson scattering profile of 2 pixels, corresponding to 0.3 cm (Table I). The spatial calibration procedure yields a similar uncertainty in the peak location (Sec. V A). Motion of the plasma during the ENDD exposure and in the time between Thomson scattering pulses is estimated to contribute an uncertainty of 1 cm (Sec. V B 3). Balmer-β emission from molecular processes may be of comparable importance in determining the peak location, resulting in a shift of 2 cm in one simulation (Sec. VI B 2).

None of these uncertainties, however, can fully account for the largest deviations between the simulated and observed peak locations, $\Delta R = R_{\mathrm{ENDD}} - R_{\mathrm{DEGAS2}} \leq 4$ cm. Note that the simulated peak locations R_{DEGAS2} consistently track the steep gradient region in the plasma profiles (R_{100}; Fig. 4); simulations of GPI did likewise.[58]. In contrast, the observed peak locations R_{ENDD} vary much less with R_{100}. As a result, the two simulations with the largest ΔR have R_{ENDD} well outside R_{100}, placing the D_β emission peak in a region with $T_e < 20$ eV. As can be seen from Eq. (1), the location of the emission peak is determined by the competition between the inward gradient of the $n = 4$ population coefficient (increasing with plasma parmeters) and the outward gradient of the neutral density due to ionization. Since this balance is purely a function of the plasma parameters, a peak at such low T_e is incompatible with the atomic Balmer-β emission obtained from our collisional radiative model.

Molecular contributions would be larger at such T_e and may explain the large ΔR cases. However, we cannot adequately determine their magnitude without more accurate plasma parameter data; a well tested atomic physics model is also required. Unaccounted-for issues in the camera calibration (vignetting, blue shifting, mirror coatings) are a second possibility. Because of the time lapse since these experiments, more refined estimates of them cannot be made. A camera sensitivity that decreases more strongly with smaller R than that shown in Fig. 7 would also account for the apparent correlation of peak emissivity with R_{100} in Fig. 4.

Even the largest ΔR in our simulations is relatively small compared with the width of

the SOL and the scale lengths of the deuterium atom density profiles in the SOL. With this in mind, assuming that the measured ENDD peak brightness is accurate, we contend that we can use the simulated neutral density profiles as at least a first order approximation to the actual ones.

The simulated molecular densities near the vessel wall range from 2×10^{17} to 9×10^{17} m^{-3}. If we include only simulations with $\Delta R \leq 1$ cm, the lower end of this range becomes 4×10^{17} m^{-3}. The maximum atom densities are roughly an order of magnitude smaller, 1×10^{16} to 7×10^{16} m^{-3}; restricting the set with $\Delta R \leq 1$ cm moves the lower end of the range to 2×10^{16} m^{-3}. The restricted ranges also happen to be comparable to those found in the Monte Carlo sampling of the Thomson scattering profile in the simulation of shot 142214 (Fig. 6).

The D atom density in the vicinity of the ENDD peak is essentially fixed (for a particular CR model) by the calibration procedure. The neutral profiles elsewhere, where they contribute less to the ENDD signal, are more sensitive to the input data and simulation assumptions than is the ENDD brightness profile. The most relevant uncertainties established in Sec. VI are:

1. Inclusion of D_β emission from molecular processes reduces both molecular and atomic densities at the vessel wall by 35 to 50%.

2. Variations in the wall model alter D_2 and D densities by $\sim 20\%$ and $\sim 10\%$, respectively.

3. Most of the simulations with a localized neutral source yield densities within a factor of two of the baseline.

4. The Monte Carlo sampling of a single Thomson scattering profile produces standard deviations in the maximum D_2 and D densities of 12% and 26%, respectively.

Combining these directly into a single rms uncertainty is not warranted given their disparate and non-random (at least for molecular D_β emission) nature. Rather we suggest an estimated envelope of a factor of two for all effects.

Because of its insensitivity to simulation assumptions, the ENDD signal tells us more about the integrated source strength and the plasma profiles than it does about the source distribution. One might have expected to gain some insight into the nature of the neutral

source from a correlation of the peak emissivity or neutral densities with other observables. For example, a correlation with the edge D^+ density might suggest that the source is dominated by main chamber recycling. Or, if the neutral density tracked the divertor D_α, one could argue for a source tied to divertor recycling. But, no such relationships are apparent in the limited set of data examined here. More definitive conclusions will require a comprehensive database and routine determination of the neutral density profiles.

Without such knowledge, we can make no inferences regarding what these inferred neutral density profiles tell us about the densities at other locations around the torus. The bays in which the high harmonic fast wave antenna or neutral beam armor[59] are placed may have neutral densities near the wall substantially different from the ones obtained here via the ENDD view, which passes in front of an empty gap between the upper and lower passive plates (Fig. 1). As was noted in Ref. 15, little insight into this question can be obtained via the various micro-ion gauges because of the relatively low midplane neutral pressures.

ACKNOWLEDGMENTS

The authors wish to acknowledge P. W. Ross and A. L. Roquemore for the design, construction, and installation of the ENDD diagnostic. We also would like to thank D. Reiter for his assistance in compiling the data for the molecular emission processes. This work is supported by U.S. DOE Contracts DE-AC02-09CH11466 (PPPL) and DE-AC52-07NA27344 (LLNL).

REFERENCES

[1]R. L. Boivin, J. A. Goetz, A. E. Hubbard, J. W. Hughes, I. H. Hutchinson, J. H. Irby, B. LaBombard, E. S. Marmar, C. S. Mossessian, Pitcher, J. L. Terry, B. A. Carreras, and L. W. Owen, Phys. Plasmas **7**, 1919 (2000).

[2]M. A. Mahdavi, R. Maingi, R. J. Groebner, A. W. Leonard, T. H. Osborne, and G. Porter, Phys. Plasmas **10**, 3984 (2003).

[3]D. A. Russell, J. R. Myra, and D. A. D'Ippolito, Phys. Plasmas **16**, 122304 (2009).

[4]S. S. Medley, N. N. Gorelenkov, R. Andre, R. E. Bell, D. S. Darrow, E. D. Fredrickson,

S. M. Kaye, B. P. LeBlanc, A. L. Roquemore, and the NSTX Team, Nucl. Fusion **44**, 1158 (2004).

[5]P. W. Ross, *Ion power balance in neutral beam heated discharges on the National Spherical Torus Experiment (NSTX)*, Ph.D. thesis, Princeton University (2010).

[6]P. C. Stangeby, J. Nucl. Mater. **415**, S278 (2011).

[7]R. E. Bell, R. Andre, S. M. Kaye, R. A. Kolesnikov, B. P. LeBlanc, G. Rewoldt, W. X. Wang, and S. A. Sabbagh, Phys. Plasmas **17**, 082507 (2010).

[8]R. D. Bengston, P. M. Valanju, A. Ouroua, and W. L. Rowan, Rev. Sci. Instrum. **61**, 3110 (1990).

[9]R. J. Colchin, R. Maingi, M. E. Fenstermacher, T. N. Carlstrom, R. C. Isler, L. W. Owen, and R. J. Groebner, Nucl. Fusion **40**, 175 (2000).

[10]J. Harhausen, A. Kallenbach, C. Fuchs, and the ASDEX Upgrade Team, Plasma Phys. Control. Fusion **53**, 025002 (2011).

[11]L. C. Johnson and E. Hinnov, J. Quant. Spectrosc. Radiat. Transfer **13**, 333 (1973).

[12]R. E. Bell, Rev. Sci. Instrum. **66**, 558 (1995).

[13]J. H. Nichols, M. A. Jaworski, R. Kaita, T. Abrams, C. H. Skinner, and D. P. Stotler, J. Nucl. Mater. (2015).

[14]M. V. Umansky, S. I. Krasheninnikov, B. LaBombard, and J. L. Terry, Phys. Plasmas **5**, 3373 (1998).

[15]D. P. Stotler, F. Scotti, R. E. Bell, B. P. LeBlanc, and R. Raman, J. Nucl. Mater. **463**, 897 (2015).

[16]B. Cao, D. P. Stotler, S. J. Zweben, M. Bell, A. Diallo, and B. P. LeBlanc, Fusion Sci. Tech. **64**, 29 (2013).

[17]D. P. Stotler and C. F. F. Karney, Contrib. Plasma Phys. **34**, 392 (1994).

[18]D. P. Stotler, J. Boedo, B. LeBlanc, R. J. Maqueda, and S. J. Zweben, J. Nucl. Mater. **363–365**, 688 (2007).

[19]L. L. Lao, H. St. John, R. D. Stambaugh, A. G. Kellmann, and W. Pfeiffer, Nucl. Fusion **25**, 1611 (1985).

[20]S. A. Sabbagh, S. M. Kaye, J. Menard, F. Paoletti, M. Bell, R. E. Bell, J. M. Bialek, M. Bitter, E. D. Fredrickson, D. A. Gates, A. H. Glasser, H. Kugel, L. L. Lao, B. P. LeBlanc, R. Maingi, R. J. Maqueda, E. Mazzucato, D. Mueller, M. Ono, S. F. Paul, M. Peng, C. H. Skinner, D. Stutman, G. A. Wurden, W. Zhu, and NSTX Research Team,

Nucl. Fusion **41**, 1601 (2001).

[21]B. P. LeBlanc, R. E. Bell, D. W. Johnson, D. E. Hoffman, D. C. Long, and R. W. Palladino, Rev. Sci. Instrum. **74**, 1659 (2003).

[22]D. S. Darrow, Rev. Sci. Instrum. **79**, 023502 (2008).

[23]R. Raman, H. W. Kugel, T. Provost, R. Gernhardt, T. R. Jarboe, and M. G. Bell, Rev. Sci. Instrum. **74**, 1900 (2003).

[24]J. C. Weisheit, J. Phys. B **8**, 2556 (1975).

[25]R. K. Janev and J. J. Smith, At. Plasma-Mater. Interaction Data Fus. **4**, 1 (1993), supplement to the journal Nucl. Fus.

[26]I. Bray and A. T. Stelbovics, Phys. Rev. A **46**, 6995 (1992).

[27]I. Bray, D. V. Fursa, A. S. Kadyrov, A. T. Stelbovics, A. S. Kheifets, and A. M. Mukhamedzhanov, Phys. Rep. **520**, 135 (2012).

[28]D. P. Stotler, B. LaBombard, J. L. Terry, and S. J. Zweben, J. Nucl. Mater. **313–316**, 1066 (2003).

[29]D. P. Stotler, C. H. Skinner, R. V. Budny, A. T. Ramsey, D. N. Ruzic, and R. B. Turkot, Jr., Phys. Plasmas **3**, 4084 (1996).

[30]K. Sawada and T. Fujimoto, J. Appl. Phys. **78**, 2913 (1995).

[31]T. Fujimoto, K. Sawada, and K. Takahata, J. Appl. Phys. **66**, 2315 (1989).

[32]R. K. Janev, W. D. Langer, K. Evans, Jr., and D. E. Post, Jr., *Elementary Processes in Hydrogen-Helium Plasmas*, Springer Series on Atoms and Plasmas (Springer-Verlag, New York, 1987).

[33]S. J. Zweben, R. Maqueda, D. P. Stotler, A. Keesee, J. Boedo, C. Bush, S. Kaye, B. LeBlanc, J. Lowrance, V. Mastrocola, R. Maingi, N. Nishino, G. Renda, D. Swain, J. Wilgen, and the NSTX Team, Nucl. Fusion **44**, 134 (2004).

[34]S. J. Zweben, W. M. Davis, S. M. Kaye, J. R. Myra, R. E. Bell, B. P. LeBlanc, R. J. Maqueda, T. Munsat, S. A. Sabbagh, Y. Sechrest, D. P. Stotler, and the NSTX Team, Nucl. Fusion (2015).

[35]R. Maingi, K. Tritz, E. D. Fredrickson, J. E. Menard, S. A. Sabbagh, D. Stutman, M. G. Bell, R. E. Bell, C. E. Bush, D. A. Gates, D. W. Johnson, R. Kaita, S. M. Kaye, H. W. Kugel, B. P. LeBlanc, D. Mueller, R. Raman, A. L. Roquemore, and V. A. Soukhanovski, Nucl. Fusion **45**, 264 (2005).

[36]R. Maingi, T. H. Osborne, B. P. LeBlanc, R. E. Bell, J. Manickam, P. B. Snyder, J. E.

Menard, D. K. Mansfield, H. W. Kugel, R. Kaita, S. P. Gerhardt, S. A. Sabbagh, F. A. Kelly, and N. research team, Phys. Rev. Lett. **103**, 075001 (2009).

[37]Y. Marandet, P. Tamain, R. Futtersack, P. Ghendrih, P. Genesio, and A. Mekkaoui, J. Nucl. Mater. **438**, S518 (2013).

[38]J.-W. Ahn, F. Scotti, K. Kim, J. M. Canik, J. D. Lore, R. Maingi, A. G. McLean, R. E. Bell, A. Diallo, S. P. Gerhardt, T. K. Gray, S. M. Kaye, B. P. LeBlanc, V. A. Soukhanovskii, and K. Tritz, Plasma Phys. Control. Fusion **56**, 015005 (2014).

[39]M. G. Bell, H. W. Kugel, R. Kaita, L. E. Zakharov, H. Schneider, B. P. LeBlanc, D. Mansfield, R. E. Bell, R. Maingi, S. Ding, S. M. Kaye, S. F. Paul, S. P. Gerhardt, J. M. Canik, J. C. Hosea, G. Taylor, and the NSTX Research Team, Plasma Phys. Control. Fusion **51**, 124054 (2009).

[40]F. Scotti, V. A. Soukhanovskii, S. Bell, R. E.and Gerhardt, W. Guttenfelder, S. Kaye, R. Andre, A. Diallo, R. Kaita, B. P. LeBlanc, M. Podesta, and the NSTX Team, Nucl. Fusion **53**, 083001 (2013).

[41]S. D. Loch, C. P. Ballance, M. S. Pindzola, and D. P. Stotler, Plasma Phys. Control. Fusion **51**, 105006 (2009).

[42]D. Reiter, P. Bogen, and U. Samm, J. Nucl. Mater. **196–198**, 1059 (1992).

[43]P. T. Greenland, J. Nucl. Mater. **290–293**, 615 (2001).

[44]U. Fantz, D. Reiter, B. Heger, and D. Coster, J. Nucl. Mater. **290–293**, 367 (2001).

[45]R. J. Goldston, Plasma Phys. **20**, 1199 (1978).

[46]M. B. Tendler and Ågren, Phys. Fluids **25**, 1037 (1982).

[47]B. Lehnert, Nucl. Fusion **23**, 1327 (1983).

[48]K. F. Alexander, K. Günther, W. Hintze, M. Laux, P. Pech, H.-D. Reiner, and A. V. Chankin, Nucl. Fusion **26**, 1575 (1986).

[49]P. S. Krstic and D. R. Schultz, At. Plasma-Mater. Data Fus. **8**, 1 (1998), supplement to the journal Nucl. Fus.

[50]R. J. Kanzleiter, D. P. Stotler, C. F. F. Karney, and D. Steiner, Phys. Plasmas **8**, 5064 (2000).

[51]P. C. Stangeby, *The Plasma Boundary of Magnetic Fusion Devices* (Institute of Physics Publishing, Philadelphia, 2000).

[52]G. Haas, P. Bachmann, D. Düchs, R. Reichle, D. Reiter, and R. Schneider, J. Nucl. Mater. **196–198**, 481 (1992).

[53]S. Lisgo, P. Börner, C. Boswell, D. Elder, B. LaBombard, B. Lipschultz, C. S. Pitcher, D. Reiter, P. C. Stangeby, J. L. Terry, and S. Wiesen, J. Nucl. Mater. **337–339**, 139 (2005).

[54]D. P. Stotler, Physica Scripta **T124**, 23 (2006).

[55]K. Schmid, J. Nucl. Mater. **438**, S484 (2013).

[56]C. H. Skinner, R. Sullenberger, B. E. Koel, M. A. Jaworski, and H. W. Kugel, J. Nucl. Mater. **438**, S647 (2013).

[57]W. Eckstein, *Computer simulations of ion-solid interactions* (Springer-Verlag, New York, 1991).

[58]S. J. Zweben, D. P. Stotler, R. E. Bell, W. M. Davis, S. M. Kaye, B. P. LeBlanc, R. J. Maqueda, E. T. Meier, T. Munsat, Y. Ren, S. A. Sabbagh, Y. Sechrest, D. R. Smith, and V. Soukhanovskii, Plasma Phys. Control. Fusion **56**, 095010 (2014).

[59]M. Ono, S. M. Kaye, Y.-K. M. Peng, G. Barnes, W. Blanchard, M. D. Carter, J. Chrzanowski, L. Dudek, R. Ewig, D. Gates, R. E. Hatcher, T. Jarboe, S. C. Jardin, D. Johnson, R. Kaita, M. Kalish, C. E. Kessel, H. W. Kugel, R. Maingi, R. Majeski, J. Manickam, B. McCormack, J. Menard, D. Mueller, B. A. Nelson, B. E. Nelson, C. Neumeyer, G. Oliaro, F. Paoletti, R. Parsells, E. Perry, N. Pomphrey, S. Ramakrishnan, R. Raman, G. Rewoldt, J. Robinson, A. L. Roquemore, P. Ryan, S. Sabbagh, D. Swain, E. J. Synakowski, M. Viola, M. Williams, W. J. R., and N. Team, Nucl. Fusion **40**, 557 (2000).